



## Performance, structure, and mechanism of CeO<sub>2</sub> in HCl oxidation to Cl<sub>2</sub>

A. P. Amrute,<sup>a</sup> C. Mondelli,<sup>a</sup> M. Moser,<sup>a</sup> G. Novell-Leruth,<sup>b</sup>

N. López,<sup>b</sup> D. Rosenthal,<sup>c</sup> R. Farra,<sup>c</sup> M. E. Schuster,<sup>c</sup> D. Teschner,<sup>c,d</sup> T. Schmidt,<sup>c</sup> J. Pérez-Ramírez<sup>a,\*</sup>

<sup>a</sup>Institute for Chemical and Bioengineering, Department of Chemistry and Applied Biosciences, ETH Zurich, Wolfgang-Pauli-Strasse 10, CH-8093 Zurich, Switzerland.

<sup>b</sup>Institute of Chemical Research of Catalonia (ICIQ), Av. Països Catalans 16, 43007 Tarragona, Spain.

<sup>c</sup>Fritz-Haber Institute of the Max Planck Society, D-14159 Berlin, Germany.

<sup>d</sup>Institute of Isotopes, Hungarian Academy of Science, H-1525 Budapest, Hungary.

<sup>e</sup>Bayer MaterialScience AG, PUR-PTI-PRI, Chempark B598, D-41538 Dormagen, Germany.

\* Corresponding author: e-mail [jpr@chem.ethz.ch](mailto:jpr@chem.ethz.ch),

Received 9 August 2011; Revised 20 November 2011; Accepted 22 November 2011; Available online 26 December 2011

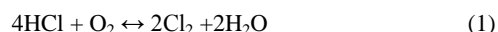
### Abstract

Experimental and theoretical studies reveal performance descriptors and provide molecular-level understanding of HCl oxidation over CeO<sub>2</sub>. Steady-state kinetics and characterization indicate that CeO<sub>2</sub> attains a significant activity level, which is associated with the presence of oxygen vacancies. Calcination of CeO<sub>2</sub> at 1173 K prior to reaction maximizes both the number of vacancies and the structural stability of the catalyst. X-ray diffraction and electron microscopy of samples exposed to reaction feeds with different O<sub>2</sub>/HCl ratios provide evidence that CeO<sub>2</sub> does not suffer from bulk chlorination in O<sub>2</sub>-rich feeds (O<sub>2</sub>/HCl ≥ 0.75), while it does form chlorinated phases in stoichiometric or sub-stoichiometric feeds (O<sub>2</sub>/HCl ≤ 0.25). Quantitative analysis of the chlorine uptake by thermogravimetry and X-ray photoelectron spectroscopy indicates that chlorination under O<sub>2</sub>-rich conditions is limited to few surface and sub-surface layers of CeO<sub>2</sub> particles, in line with the high energy computed for the transfer of Cl from surface to sub-surface positions. Exposure of chlorinated samples to a Deacon mixture with excess oxygen rapidly restores the original activity levels, highlighting the dynamic response of CeO<sub>2</sub> outermost layers to feeds of different composition. Density functional theory simulations reveal that Cl activation from vacancy positions to surface Ce atoms is the most energy-demanding step, although chlorine-oxygen competition for the available active sites may render re-oxidation as the rate-determining step. The substantial and remarkably stable Cl<sub>2</sub> production and the lower of CeO<sub>2</sub> make it an attractive alternative to RuO<sub>2</sub> for catalytic chlorine recycling in industry.

**Keywords:** Chlorine recycling; HCl oxidation; CeO<sub>2</sub>; Oxygen vacancies; Chlorination.

### 1. Introduction

The heterogeneously catalyzed gas-phase oxidation of HCl to Cl<sub>2</sub> (Eq. (1)) is a sustainable route to recycle chlorine from by-product HCl streams derived from the manufacture of polyurethanes and polycarbonates with low energy input [1,2]. The amount of waste HCl raises due to the growing demand for these versatile plastics. As selling the HCl excess is unfeasible, and the neutralization option is unattractive, its catalytic conversion to Cl<sub>2</sub> is receiving an increasing interest.



Since its introduction and till recent times, the industrialization of HCl oxidation has suffered from many failed attempts to obtain sufficiently active and durable catalysts. The CuCl<sub>2</sub>/pumice catalyst patented by Henry Deacon in 1868 [3] exhibited fast deactivation due to volatilization of the active phase in the form of copper chlorides. Later examples of processes of limited success are the Shell-Chlor

process (based on CuCl<sub>2</sub>-KCl/SiO<sub>2</sub>) [4] and the Mitsui-Toatsu process (based on Cr<sub>2</sub>O<sub>3</sub>/SiO<sub>2</sub> as catalyst) [5]. Only recently, ruthenium supported on specific carriers was successfully developed for large-scale chlorine recycling [1]. In particular, Sumitomo has applied RuO<sub>2</sub>/SiO<sub>2</sub>/TiO<sub>2</sub>-rutile in a plant producing 100 kton Cl<sub>2</sub> per year [2,6], while Bayer's RuO<sub>2</sub>/SnO<sub>2</sub>-Al<sub>2</sub>O<sub>3</sub> catalyst has been piloted and is ready for industrial use [7,8]. The distinctive features of RuO<sub>2</sub>-based catalysts are the high activity at low temperature and the remarkable stability against bulk chlorination [9-11].

The implementation of catalytic HCl oxidation technology would expand if cheaper, but comparably stable, alternatives to RuO<sub>2</sub>-based catalysts were developed. The high and fluctuating market price of ruthenium indeed reflects in large costs for new plants [12]. These considerations have constituted the driving force to develop alternative cost-effective catalytic materials. A first step in this direction is the recent design of a copper delafossite (CuAlO<sub>2</sub>) catalyst, which exhibited stable performance for more than 1,200 hours on stream [13]. However, this catalyst experienced significant copper loss.

CeO<sub>2</sub> (fluorite structure [14]) attracted our interest in view of its wide use in redox processes in many research fields [15-21], and oxidation reactions in particular [22-26]. In oxidations, it has been employed both as catalyst and co-catalyst. The success of CeO<sub>2</sub> is due to the easy generation of oxygen vacancies [22,27,28], which facilitate activation and transport of oxygen species. Nevertheless, only a few works have derived quantitative correlations between its oxidation activity and this structural peculiarity, typically measured in terms of oxygen storage capacity (OSC). Furthermore, comparisons have been preferably reported between CeO<sub>2</sub> and solid solutions of CeO<sub>2</sub> with ZrO<sub>2</sub> or SiO<sub>2</sub> [29], or between ceria-containing catalysts including supported (active) metal phases [30].

CeO<sub>2</sub>-based materials have been claimed in the patent literature as catalysts potentially suited for HCl oxidation [31-33]. However, there are no studies gathering a fundamental understanding of the Deacon chemistry on CeO<sub>2</sub>. Only the detailed assessment of CeO<sub>2</sub> activity and stability will determine its potential as an alternative to RuO<sub>2</sub>-based catalysts for HCl oxidation.

Herein we report on the use of CeO<sub>2</sub> in HCl oxidation, as well as on the fundamental knowledge gathered by means of a multi-technique approach. Performance-structure-mechanism relationships are established, collecting information from extensive kinetic tests in a flow reactor at ambient pressure, detailed characterization (in relation to the catalyst preparation procedure and the operating conditions), and mechanistic investigations using *in situ* infrared spectroscopy and density functional theory calculations.

**Table 1.** Description of catalysts' codes.

Catalyst code	Calcination temperature (K)	Catalyst state (-)	Feed O <sub>2</sub> /HCl ratio (mol mol <sup>-1</sup> )
CeO <sub>2</sub> -573-F	573	fresh	-
CeO <sub>2</sub> -773-F	773	fresh	-
CeO <sub>2</sub> -1023-F	1023	fresh	-
CeO <sub>2</sub> -1173-F	1173	fresh	-
CeO <sub>2</sub> -1273-F	1273	fresh	-
CeO <sub>2</sub> -1373-F	1373	fresh	-
CeO <sub>2</sub> -573-2	573	used	2
CeO <sub>2</sub> -773-2	773	used	2
CeO <sub>2</sub> -1023-2	1023	used	2
CeO <sub>2</sub> -1173-2	1173	used	2
CeO <sub>2</sub> -1273-2	1273	used	2
CeO <sub>2</sub> -1373-2	1373	used	2
CeO <sub>2</sub> -773-0	773	used	0
CeO <sub>2</sub> -1173-0	1173	used	0
CeO <sub>2</sub> -1173-0.25	1173	used	0.25
CeO <sub>2</sub> -1173-0.75	1173	used	0.75
CeO <sub>2</sub> -1173-0.25-2	1173	used	0.25 followed by 2
CeO <sub>2</sub> -1173-0.25-7	1173	used	0.25 followed by 7
CeO <sub>2</sub> -1173-0-7	1173	used	0 followed by 7

## 2. Experimental

### 2.1. Catalysts

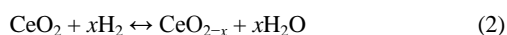
CeO<sub>2</sub> (Aldrich, nanopowder, code 544841) was calcined in static air at various temperatures in the range of 573-1373 K using a heating rate of 10 K min<sup>-1</sup> and a dwell time of 5 h prior to use. The thus obtained samples are referred to as 'fresh'. A complete list of all samples codes used along the manuscript, together with their description, is reported in Table 1.

### 2.2. Characterization

All the samples were subjected to basic characterization prior to and after catalytic testing. More extensive characterization was performed on CeO<sub>2</sub>-773 and CeO<sub>2</sub>-1173. In particular, fresh samples of these two catalysts were compared to samples exposed to reaction mixtures with feed O<sub>2</sub>/HCl ratios equal to 2, 0.75, 0.25, or 0 (see Section 2.3 for detailed testing conditions).

Standard characterization of the samples was performed by powder X-ray diffraction (XRD), nitrogen adsorption at 77 K, and temperature-programmed reduction with hydrogen (H<sub>2</sub>-TPR). The oxygen storage capacity (OSC) was measured by estimating the H<sub>2</sub> uptake of the samples (after a similar pre-treatment in inert gas as prior to the catalytic evaluation), as this represents an indirect quan-

tification of the oxygen that the samples can store (Eq. (2)) [34-36].



This method was chosen among others reported in the literature [37], as the straightforward approach of determining the OSC by pulse chemisorption of oxygen [38] did not provide reproducible results. In order to select the appropriate temperature (573 K), at which the OSC would be evaluated in relation to a few outermost surface layers of CeO<sub>2</sub>, the H<sub>2</sub> uptake was first separately measured at various temperatures (523-873 K), defined on the basis of the H<sub>2</sub>-TPR profiles (Figs. S1-S2 in the ESI). The degree of bulk chlorination of selected catalysts after HCl oxidation was determined by thermogravimetric analysis coupled to mass spectrometry (TGA-MS). The structure, morphology, and composition of the catalyst particles were studied by high-resolution transmission electron microscopy (HRTEM). X-ray photoelectron spectroscopy (XPS) was applied to determine the degree of chlorination of the used CeO<sub>2</sub> catalysts. Three different layer models were employed to calculate the number of layers in CeO<sub>2</sub> that experienced chlorination. The first model was based on the inelastic mean free path (IMFP) and on 100% Cl occupation, the second on 80% of IMFP for practical effective attenuation length (EAL) and on 100% Cl occupation, and the third 80% of IMFP for practical EAL and on 75% Cl occupation. For details on the characterization techniques, the reader is referred to the electronic supplementary information (ESI).

### 2.3. Catalytic tests

The oxidation of HCl with O<sub>2</sub> was screened at ambient pressure in a quartz fixed-bed micro-reactor (8 mm i.d.) using 0.5 g of catalyst (sieve fraction = 0.4-0.6 mm), a total flow of 166 cm<sup>3</sup> STP min<sup>-1</sup>, a bed temperature ( $T_{\text{bed}}$ ) of 703 K, and reaction times up to 3 h. A mixture containing 10 vol.% HCl (Messer, purity 2.8, anhydrous) and 20 vol.% O<sub>2</sub> (Pan Gas, purity 5.0), balanced in N<sub>2</sub> (Pan Gas, purity 5.0) was fed.

Steady-state kinetic studies were performed on CeO<sub>2</sub>-1173-F. First of all, it was experimentally verified that, under our experimental conditions, the reaction was not limited by extra- and/or intra-particle diffusion limitations. For this purpose, we varied (i) the total flow rate (83-250 cm<sup>3</sup> STP min<sup>-1</sup>) at constant space time ( $W/F^0(\text{HCl}) = 11.2 \text{ g h mol}^{-1}$ , defined as the ratio of the catalyst mass to the inlet molar flow of HCl) and (ii) the average particle size (0.14-0.5 mm) with other conditions constant, respectively (Fig. S3 in the ESI). The kinetic experiments included changes of the feed composition at different temperatures and space times. In particular, the O<sub>2</sub>/HCl ratio was varied in the range of 0.5-7 at constant feed HCl concentration (10 vol.%) and in the range 0.25-2

at constant feed O<sub>2</sub> concentration (10 vol.%) at  $T_{\text{bed}} = 603, 653, \text{ and } 703 \text{ K}$  and at space times of 5.6, 9, and 11.2 g h mol<sup>-1</sup>. CeO<sub>2</sub>-1173-F samples exposed to O<sub>2</sub>/HCl = 0, 0.25, or 0.75 at 703 K for 3 h, and CeO<sub>2</sub>-773-F treated in O<sub>2</sub>/HCl = 0 (only HCl) at 703 K for 3 h were collected for characterization, after switching the feed to inert gas and allowing the reactor to cool down. Experiments were carried out at 703 K also combining a HCl-rich step, in which the catalyst was exposed to a feed composition O<sub>2</sub>/HCl = 0 or 0.25 (causing bulk chlorination), and a O<sub>2</sub>-rich step, in which substantial oxygen excess was supplied (O<sub>2</sub>/HCl = 2 or 7). These tests enable to study catalyst re-oxidation. Cl<sub>2</sub> quantification at the reactor outlet was carried out by iodometric titration in a Mettler Toledo G20 Compact Titrator, using the protocol reported elsewhere [39]. HCl conversion was determined from the Cl<sub>2</sub> produced, taking into account the reaction stoichiometry.

### 2.4. In situ Fourier transform infrared spectroscopy

A home-made transmission cell, especially designed to withstand the corrosive HCl oxidation mixture, was used for in situ Fourier transform infrared (FTIR) spectroscopy measurements. The sample in powder form was pressed into a self-supporting disc (15 mg cm<sup>-2</sup>) under 30 bar for 10 s. The wafer, having a thickness of 50 μm, was placed in the sample holder, which also serves as the heating system. Inlet gases were analytical grade and controlled by mass flow controllers. The sample was heated in 20 vol.% O<sub>2</sub> in N<sub>2</sub> (100 cm<sup>3</sup> STP min<sup>-1</sup>) up to 653 K (5 K min<sup>-1</sup>), and allowed to stabilize. After ca. 1 h, 1 vol.% HCl was introduced into the O<sub>2</sub>/N<sub>2</sub> flow to mimic a diluted Deacon feed condition. Spectra were recorded with a Varian-670 FTIR spectrometer at 653 K and with 4 cm<sup>-1</sup> resolution.

### 2.5. Computational details

Density functional theory (DFT) simulations was applied to CeO<sub>2</sub> slabs. The calculations were performed with the 5.2 version of the VASP code [40]. The functional of choice was a GGA+U scheme to account in an approximate way for the complexity arising from the presence of *f*-electrons in cerium. The GGA was PBE [41], the U parameter chosen was set to 4.5 [42,43], and the inner electrons were replaced by PAW pseudopotentials [44]. The 12 valence electrons of Ce atoms in the 5*s*, 5*p*, 6*s*, 4*f*, and 5*d* states and the 6 valence electrons of O atoms in the 2*s*, and 2*p* states were considered explicitly. The valence electrons were expanded in plane waves with a cut off energy of 400 eV. For the bulk, the k-point sampling was 9×9×9 [45]. The cell parameter obtained for the bulk was 5.486 Å, in good agreement with experimental results and previous calculations [42,43]. The (111) facet was selected for the study as it is known to be the lowest energy surface [43].

The chosen slab corresponds to a  $p(2\times 2)$  reconstruction and contains 3 layers. The k-point sampling was set to  $3\times 3\times 1$  in this case. The calculated surface energy for this structure was  $0.013\text{ eV \AA}^{-2}$ . For this surface, several vacancy structures were considered and benchmarked against more accurate calculations in the literature employing hybrid methods [43]. When forming a vacancy or adsorbing on this surface, the systems were allowed to relax in all directions, except for the last layer of the slab. In all cases, the slabs were interleaved by  $10\text{ \AA}$  and decoupled from electronic interactions due to spurious polarizations given the asymmetry of the adsorption configuration. Spin-polarized calculations were performed when required. The CI-NEB method [46] was employed to locate the transition states, and the vibrational analysis of the potential transition state structures was performed to fully characterize the saddle points. In the calculation of vibrational frequencies, only the adsorbed structures of intermediates or transition states were considered. The numerical Hessian was calculated with two steps of  $0.02\text{ \AA}$  for each degree of freedom and then diagonalized to obtain the corresponding eigenvalues and eigenmodes.

### 3. Results and discussion

#### 3.1. Catalytic evaluation

##### 3.1.1. Influence of calcination temperature on activity

CeO<sub>2</sub> samples calcined at different temperatures were tested in the gas-phase catalytic oxidation of HCl in a continuous-flow fixed-bed reactor operated at ambient pressure and under isothermal conditions. XRD analyses showed that the fresh samples exhibited the characteristic reflections of cerium(IV) oxide. The HCl conversion over the samples ranged from 2 to 29% (Table 2), remaining essentially constant in the course of the 3-h test. Interestingly, the CeO<sub>2</sub> samples calcined at temperatures between 573 and 1173 K were similarly active, achieving the highest conversion levels, while higher calcination temperatures led to a progressive and almost complete depletion of the activity. These findings have been related to changes in the textural and structural properties of the materials and are first discussed on the basis of N<sub>2</sub> adsorption results. For the fresh catalysts, higher calcination temperatures led to lower total surface area ( $S_{\text{BET}}$ ) values (Table 2). This result is expected, as higher temperatures favor sintering of the particles. The dependence of the HCl conversion on the  $S_{\text{BET}}$  of the fresh samples is shown in Fig. 1a (open symbols). For  $S_{\text{BET}}$  values  $> 25\text{ m}^2\text{ g}^{-1}$  (i.e. calcination temperature below 1173 K), the activity is independent of the  $S_{\text{BET}}$ , while for  $S_{\text{BET}}$  values  $< 25\text{ m}^2\text{ g}^{-1}$  (i.e. calcination temperature above 1173 K), it strongly depends on the surface area. In particular, CeO<sub>2</sub>-1273-F ( $S_{\text{BET}} = 12\text{ m}^2\text{ g}^{-1}$ ) and CeO<sub>2</sub>-1373-F ( $S_{\text{BET}} = 1\text{ m}^2\text{ g}^{-1}$ ) respectively exhibited 14 and 2% HCl conversion, i.e. 2 and ca. 15 times lower activity than

**Table 2.** Characterization and catalytic activity data.

Catalyst	$S_{\text{BET}}^a$ ( $\text{m}^2\text{ g}^{-1}$ )		$X_{\text{HCl}}^b$	OSC <sup>c</sup>
	fresh	used	(%)	( $\mu\text{g O g}_{\text{cat}}^{-1}$ )
CeO <sub>2</sub> -573	117	46	29	-
CeO <sub>2</sub> -773	106	27	25	390
CeO <sub>2</sub> -1023	53	39	25	382
CeO <sub>2</sub> -1173	30	25	27	376
CeO <sub>2</sub> -1273	12	11	14	237
CeO <sub>2</sub> -1373	1	1	2.1	78

<sup>a</sup> Total surface area, BET method.

<sup>b</sup> HCl conversion at  $\text{O}_2/\text{HCl} = 2$ ,  $T_{\text{bed}} = 703\text{ K}$ ,  $P = 1\text{ bar}$ ,  $W/F^0(\text{HCl}) = 11.2\text{ g h mol}^{-1}$ .

<sup>c</sup> Oxygen storage capacity measured at 573 K.

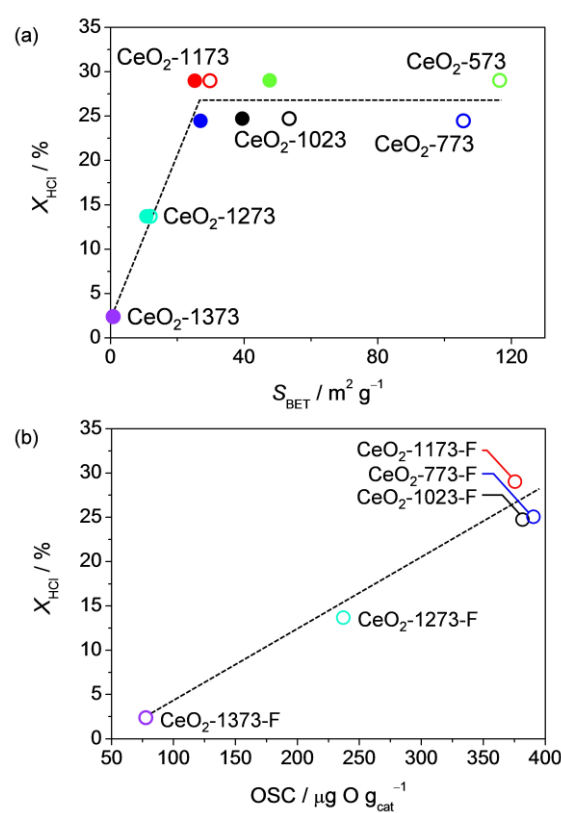


**Fig. 1.** HCl conversion versus (a) surface area of fresh (open symbols) and used (solid symbols) CeO<sub>2</sub> samples and (b) OSC, measured at 573 K, of fresh CeO<sub>2</sub> samples. Conditions: inlet mixture of 10 vol.% HCl and 20 vol.% O<sub>2</sub> balanced in N<sub>2</sub>,  $T_{\text{bed}} = 703\text{ K}$ ,  $W/F^0(\text{HCl}) = 11.2\text{ g h mol}^{-1}$ ,  $P = 1\text{ bar}$ , and time-on-stream = 3 h.

the other catalysts. Exposure of the catalysts to reaction conditions generally led to a drop in  $S_{\text{BET}}$  (Table 2). The change is significant for CeO<sub>2</sub>-573-2, CeO<sub>2</sub>-773-2, and CeO<sub>2</sub>-1023-2, evidence that significant sintering of the CeO<sub>2</sub> particles occurred during HCl oxidation. On the other hand, the  $S_{\text{BET}}$  values of CeO<sub>2</sub>-1173-2, CeO<sub>2</sub>-1273-2, and CeO<sub>2</sub>-1373-2 were hardly affected, indicating that calcination at or above 1173 K resulted in stabilized materials in HCl oxidation. Calcination of the starting CeO<sub>2</sub>

nanopowder at 1173 K provides the best compromise between performance and stability against sintering. Generally, the slope-plateau relation used to depict the dependence of activity on the  $S_{\text{BET}}$  of fresh samples turned out to be a good description for the used catalysts too (Fig. 1a, solid symbols). An experiment showing practically constant HCl conversion over CeO<sub>2</sub>-773-F in contrast to a strongly decreasing  $S_{\text{BET}}$  with time-on-stream supports the observed independence of the activity on  $S_{\text{BET}}$  for values of the latter greater than 25 m<sup>2</sup> g<sup>-1</sup> (Fig. S4 in the ESI). It was accordingly concluded that another descriptor is needed to rationalize the HCl oxidation activity of CeO<sub>2</sub>.

As mentioned in the introduction, the successful application of CeO<sub>2</sub>-based materials in catalysis as well as electrochemistry has been related to its capability to generate oxygen vacancies in the lattice [19,27]. Therefore, our CeO<sub>2</sub> samples were measured to assess their oxygen storage capacities (OSC), according to a method reported elsewhere [34]. On the basis of the values obtained (Table 2), the dependence of HCl conversion on OSC followed a linear trend (Fig. 1b). For CeO<sub>2</sub>-773-F, CeO<sub>2</sub>-1023-F, and CeO<sub>2</sub>-1173-F, i.e. samples showing the highest (and similar) activity, the OSC was estimated at ca. 390 μg O g<sub>cat</sub><sup>-1</sup>. For CeO<sub>2</sub>-1273-F and CeO<sub>2</sub>-1373-F, which exhibit decreasing HCl conversion levels, diminishing OSC values were measured, respectively equal to 237 and 78 μg O g<sub>cat</sub><sup>-1</sup>. Based on these results, the OSC proved a suitable parameter to rationalize the activity differences. Nevertheless, an influence of  $S_{\text{BET}}$  on OSC and/or a combined role of OSC and  $S_{\text{BET}}$ , when the latter is below 20 m<sup>2</sup> g<sup>-1</sup>, on the catalytic activity could be considered. In this regard, Terribile et al. [47] showed that OSC, as measured for the bulk, was independent of  $S_{\text{BET}}$ . The outcome of this study might not be directly applicable to our case, in which OSC has to be considered limitedly to the outermost surface and sub-surface layers of CeO<sub>2</sub>, where the catalytic process takes place. More generally, the OSC could be described as  $\text{OSC} = S_{\text{BET}} \rho$ , where  $\rho$  corresponds to the density of surface or near-surface oxygen vacancies. At higher temperatures, the Gibbs energy for vacancy formation decreases (see DFT results), thus favoring an increased generation of vacancies in the corresponding equilibrium conditions, but  $S_{\text{BET}}$  drops. This explains why a larger OSC, i.e. more active CeO<sub>2</sub>, is found for samples calcined at 573-1173 K.

The activity of CeO<sub>2</sub> is significantly lower than that of RuO<sub>2</sub>. Furthermore, a 40 K higher light-off temperature for Cl<sub>2</sub> evolution was determined over CeO<sub>2</sub>-1173 by temperature-programmed reaction according to the protocol described in [39]. In view of a practical use, high-temperature operation is detrimental due to thermodynamic constraints that limit the equilibrium HCl conversion [48]. Nevertheless, these restrictions can be largely overcome by employing higher pressures and inlet O<sub>2</sub>/HCl ratios, so that the degree of HCl conversion achieved still makes the development of a technical process feasible. Profiles of equilibrium HCl conversion at different total pressures and O<sub>2</sub>/HCl ratios have been included in the ESI (Fig. S5a). Our

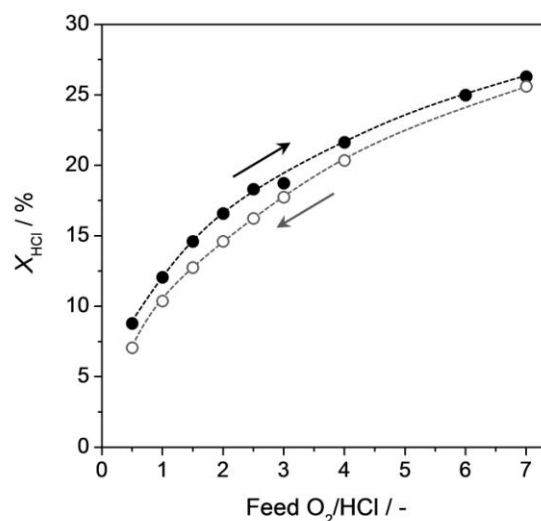


**Fig. 2.** HCl conversion versus feed O<sub>2</sub>/HCl ratio at 703 K for CeO<sub>2</sub>-1173-F. Conditions: inlet mixture of 10 vol.% HCl and 5-70 vol.% O<sub>2</sub> balanced in N<sub>2</sub>,  $T_{\text{bed}} = 703$  K,  $W/F^0(\text{HCl}) = 11.2$  g h mol<sup>-1</sup>, and  $P = 1$  bar.

experiments and calculations (vide infra) conclude that oxygen vacancies determine the activity of CeO<sub>2</sub> in HCl oxidation. More active ceria-based catalysts may be obtained enhancing its oxygen storage capacity, e.g. by addition of dopants. However, this aspect was beyond the scope of the present manuscript.

### 3.1.2. Kinetic analysis

The influence of the O<sub>2</sub>/HCl ratio on the activity was examined over CeO<sub>2</sub>-1173-F at 703 K (Fig. 2). The HCl conversion increased upon raising the relative O<sub>2</sub> content in the feed mixture. The reaction order on O<sub>2</sub>, calculated using a power equation fitting, was 0.5. This result suggests that oxygen-assisted chlorine evolution (re-oxidation) is the rate-limiting step, hence favored at a higher partial O<sub>2</sub> pressure. This point is further discussed by means of mechanistic studies by DFT in Section 3.4.3. Remarkably, the HCl conversion profiles derived from measurements in which the feed O<sub>2</sub> content was step-wise changed so to vary the O<sub>2</sub>/HCl ratio from the lowest (0.5 to 7) or from the highest (7 to 0.5) value evidence very little hysteresis. This outcome indicates that the catalyst reversibly responds to variations of the feed mixture, and highlights the dynamic character of the CeO<sub>2</sub> surface. As expected, the HCl conversion increased upon raising the space time for different feed O<sub>2</sub>/HCl ratios (Fig. S6 in the ESI). On the contrary, the Cl<sub>2</sub> production decreased upon increasing the relative feed HCl content (Fig. S7 in the ESI), thus suggesting a change in the catalyst composition at the (near-) surface level (later addressed by characterization) that leads to activity loss. With regards to the dependency of CeO<sub>2</sub> activity on the reaction temperature, the HCl conversion level varied from 1 to 18% between 603 and 703 K at O<sub>2</sub>/HCl = 2. The ap

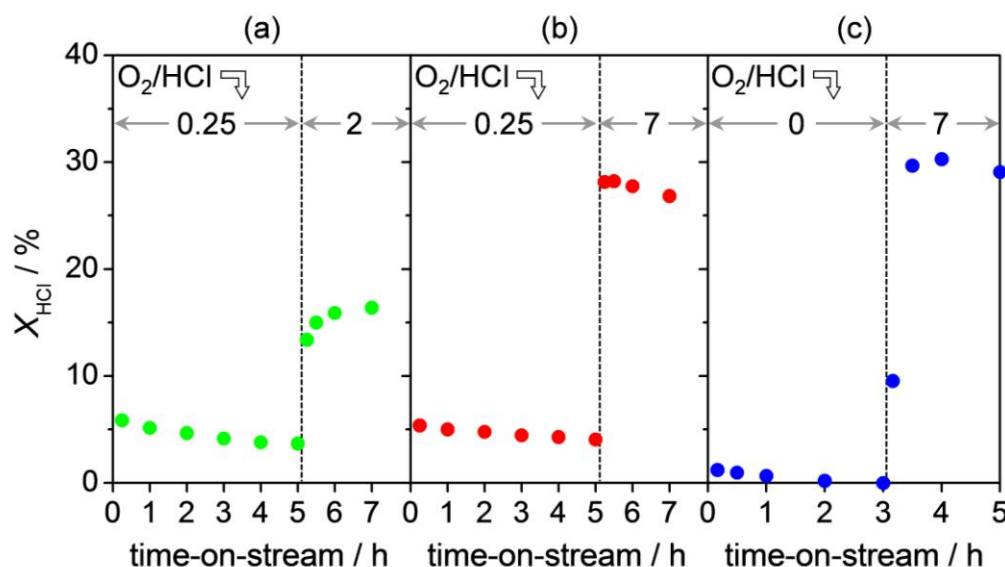


**Fig. 3.** HCl conversion *versus* time-on-stream over CeO<sub>2</sub>-1173 using sequential HCl-rich/O<sub>2</sub>-rich feed mixtures. (a) HCl-rich step with O<sub>2</sub>/HCl = 0.25 followed by O<sub>2</sub>-rich step with O<sub>2</sub>/HCl = 2. (b) HCl-rich step with O<sub>2</sub>/HCl = 0.25 followed by O<sub>2</sub>-rich step with O<sub>2</sub>/HCl = 7. (c) HCl-rich step with O<sub>2</sub>/HCl = 0 followed by O<sub>2</sub>-rich step with O<sub>2</sub>/HCl = 7. Other conditions:  $T_{\text{bed}} = 703$  K,  $W/F^0(\text{HCl}) = 11.2$  g h mol<sup>-1</sup>, and  $P = 1$  bar.

parent activation energy was estimated at ca. 90 kJ mol<sup>-1</sup>. In addition, a catalytic test using a feed mixture with O<sub>2</sub>/HCl = 5 and an increased space time (at the limit of our current set-up) was conducted. Fig. S5b in the ESI shows that a significant single-pass HCl conversion of 40% was reached over CeO<sub>2</sub> at 673 K and 1 bar.

As operation in industry would be more economic lowering the inlet partial pressure of O<sub>2</sub> down to the stoichiometric amount (O<sub>2</sub>/HCl = 0.25), we have investigated to which extent a stoichiometric or excess amount of HCl can negatively impact the catalytic activity (i.e. by chlorination). Some effort was also made to explore whether activity recovery is possible and to determine the re-oxidation kinetics. Fig. 3 displays the HCl conversion profiles obtained for CeO<sub>2</sub>-1173-F in sequential HCl-rich/O<sub>2</sub>-rich experiments under various conditions.

The HCl-rich step was conducted at 703 K using O<sub>2</sub>/HCl = 0 or 0.25 for 3 or 5 h, followed by the O<sub>2</sub>-rich step using O<sub>2</sub>/HCl = 2 or 7 for 2 h. As shown in Fig. 3a, a slight decrease in HCl conversion was observed when the reaction was carried out with O<sub>2</sub>/HCl = 0.25. Upon increasing the O<sub>2</sub> content in the feed (O<sub>2</sub>/HCl = 2), a gradual increase in activity was obtained. The HCl conversion level expected for an O<sub>2</sub>/HCl = 2 feed composition (ca. 17% HCl conversion, Fig. 2) was approached in 2 h (Fig. 3a). In view of the slow re-oxidation kinetics, the experiment was repeated at a higher O<sub>2</sub>/HCl ratio for the O<sub>2</sub>-rich step. Using O<sub>2</sub>/HCl = 7, the HCl conversion level immediately rose (Fig. 3b) to the expected value (ca. 27% HCl conversion, Fig. 2). When repeating this two-step experiment with the HCl-rich phase at O<sub>2</sub>/HCl = 0 and the O<sub>2</sub>-rich at O<sub>2</sub>/HCl = 7, a similar profile was obtained (Fig. 3c). The

data show that upon treating the catalyst with HCl in the absence of gas-phase O<sub>2</sub>, the HCl conversion was completely depleted due to excessive chlorination (*vide infra*). Nevertheless, upon switching to O<sub>2</sub>/HCl = 7, the original activity was fully restored within 1 h.

## 3.2. Characterization

### 3.2.1. X-ray diffraction and thermogravimetry

In order to relate the activity loss in HCl-rich feeds to modifications on the catalyst structure and/or composition, CeO<sub>2</sub>-1173-F samples treated at 703 K for 3 h using various O<sub>2</sub>/HCl feed ratios were analyzed by XRD (Fig. 4). The diffractogram of CeO<sub>2</sub>-773-HCl is also included for comparison purposes. For the samples exposed to O<sub>2</sub>/HCl = 0 or 0.25, CeCl<sub>3</sub>·6H<sub>2</sub>O (JCPDS 01-0149) reflections were detected, thus pointing to bulk chlorination as the main cause for the observed catalyst deactivation. From the intensity of the cerium chloride reflections, the samples could be sequenced according to the extent of bulk chlorination as follows: CeO<sub>2</sub>-773-0 > CeO<sub>2</sub>-1173-0 > CeO<sub>2</sub>-1173-0.25. The fact that CeO<sub>2</sub>-1173-HCl was less altered than CeO<sub>2</sub>-773-HCl is probably related to the better stabilization achieved by high-temperature calcination, thus not only reflecting lower sintering upon use, but also a higher resistance against chlorination. The presence of stoichiometric amounts of O<sub>2</sub> did not fully prevent structural alterations, but the degree of chlorination was smaller than for O<sub>2</sub>-free runs. Samples treated in O<sub>2</sub>/HCl = 0.75 or 2 did not suffer from detectable bulk chlorination. Accordingly,



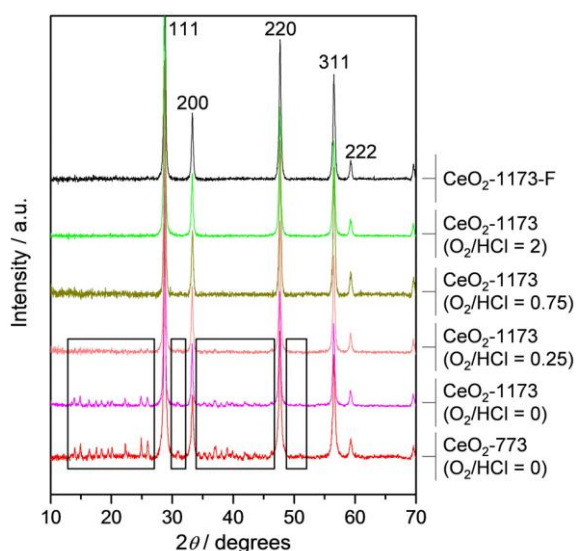


**Fig. 4.** XRD patterns of CeO<sub>2</sub>-1173 samples in fresh and used (at various O<sub>2</sub>/HCl ratios) forms. The diffractogram of CeO<sub>2</sub>-773-0 is included for comparison. The most intense reflections are due to CeO<sub>2</sub> (JCPDS 73-6328), while those within boxes belong to CeCl<sub>3</sub>·6H<sub>2</sub>O (JCPDS 01-0149).

the choice of O<sub>2</sub>/HCl feed ratio is of great importance, and should be equal or higher than 0.75 to avoid activity deterioration of CeO<sub>2</sub>-based catalysts. The inhibiting effect of excess HCl on the conversion (Fig. S7 in the ESI) can be also related to bulk chlorination. Nevertheless, deactivation does not appear to be induced by the volatilization of the active phase in form of the metal chlorides produced in situ, as in the case of copper-based catalysts [13,39]. Analysis of the filtrate by ICP-OES did not show appreciable cerium loss. On the basis of the result of the catalytic test on CeCl<sub>3</sub> (HCl conversion = 2%, at 703 K and O<sub>2</sub>/HCl = 2), the activity loss is related to the inactivity of cerium chloride for HCl oxidation.

XRD analyses of the samples exposed to the HCl-rich/O<sub>2</sub>-rich mixtures (Fig. S8 in the ESI) evidenced that activity recovery was indeed induced by removal of chlorine at higher partial pressures of O<sub>2</sub>. In the case of the samples treated with O<sub>2</sub>/HCl = 7, the original CeO<sub>2</sub> phase was fully restored, while traces of CeCl<sub>3</sub>·6H<sub>2</sub>O were still observed for the sample exposed to a lower oxygen excess (O<sub>2</sub>/HCl = 2). This evidence is in line with the activity pattern described above.

Quantification of the chlorination degree was estimated performing TGA-MS studies of the used catalysts. The weight loss and MS profiles as a function of the temperature are reported in Fig. S9 in the ESI. According to these data, the estimated values for molar Cl/Ce ratio were 0.38, 0.30, and 0.08 for CeO<sub>2</sub>-773-0, CeO<sub>2</sub>-1173-0, and CeO<sub>2</sub>-1173-0.25, respectively. These results support the trend qualitatively derived by XRD analysis.

In contrast to the extensive bulk alteration reported for CuO and MnO<sub>2</sub> already upon exposure to an O<sub>2</sub>-rich feed (O<sub>2</sub>/HCl = 2) [39,49], chlorination of CeO<sub>2</sub> occurs

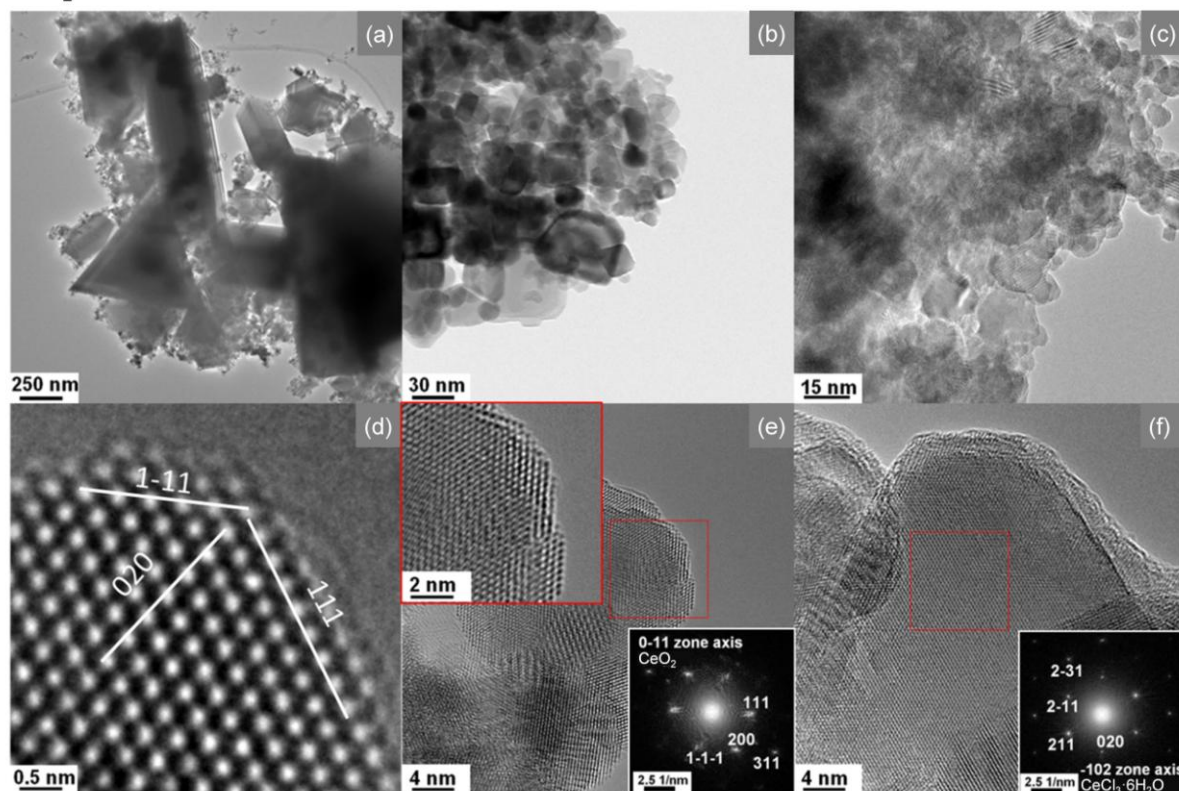
only at stoichiometric feed conditions or in excess HCl and to a very limited extent. Consequently, the behavior of CeO<sub>2</sub> resembles more that of RuO<sub>2</sub>, and this is directly related to the high stability of the latter two oxides.

### 3.2.2. High-resolution transmission electron microscopy

TEM micrographs of CeO<sub>2</sub>-773-F reveal a bimodal particle size distribution (Fig. 5a). Small CeO<sub>2</sub> particles of approximately 10 nm are scattered around larger particles reaching up to 300 nm. Exposure to O<sub>2</sub>/HCl = 2 induced a significant change in particle size (CeO<sub>2</sub>-773-2), which attained a range of 20-40 nm (Fig. 5b). Under Deacon conditions, the smaller particles agglomerated and the bigger particles “cracked”, thus not being detectable in the used sample. While sintering is expected to occur upon use, the latter phenomenon is tentatively explained on the basis of a different activity/stability of the crystal facets, where one (or more) might be unstable under reaction conditions. It cannot be excluded that the mechanical strain applied in the pressing step during preparation of the sieve fraction may be the origin of the breaking up of the bigger grains. Nevertheless, the significantly reduced S<sub>BET</sub> of CeO<sub>2</sub>-773-2 implies that the loss in surface area determined by the agglomeration of the small particles clearly surpasses the increase due to the breaking up of few big grains. High-resolution imaging of the surface of CeO<sub>2</sub> nanoparticles after exposure to Deacon conditions shows clean surfaces exhibiting several steps (Fig. 5d). The analysis of CeO<sub>2</sub>-773-0 reveals some clear changes due to the pure-HCl treatment. While the size of the nanoparticles does not seem to differ significantly from CeO<sub>2</sub>-773-2 (Fig. 5c), the treatment had a considerable effect on the particle structure. Besides rounded nanoparticles of CeO<sub>2</sub>-773-0 (Fig. 5e), revealing numerous “clean” atomic steps on the surface (magnified in the inset of Fig. 5e), nanoparticles covered with an amorphous layer are now evidenced (Fig. 5f). SAED (selected area electron diffraction) analysis of such particles suggests that the structure can fit to CeCl<sub>3</sub>·6H<sub>2</sub>O, in agreement with the structure assigned by XRD (Fig. 4). The high vacuum conditions of the TEM could result in the removal of crystal water from the CeCl<sub>3</sub>·6H<sub>2</sub>O particles, leading to a collapse of the structural order in the near-surface region. This would explain the amorphous layer near the particle surface. The co-existence of clean CeO<sub>2</sub> particles and particles covered by the chloride phase substantiates that certain crystallographic planes of CeO<sub>2</sub> are less prone to chlorination while others favor CeCl<sub>3</sub>·6H<sub>2</sub>O formation.

The catalyst morphology within the complete “1173”-series (Fig. 5g-i) looks substantially similar, with the particle size ranging between 20 and 40 nm in all the samples. The fresh catalyst does not contain considerable amounts of bigger particles as in CeO<sub>2</sub>-773-F. Thus, the particle size was stabilized already during calcination at a

### CeO<sub>2</sub>-773



### CeO<sub>2</sub>-1173

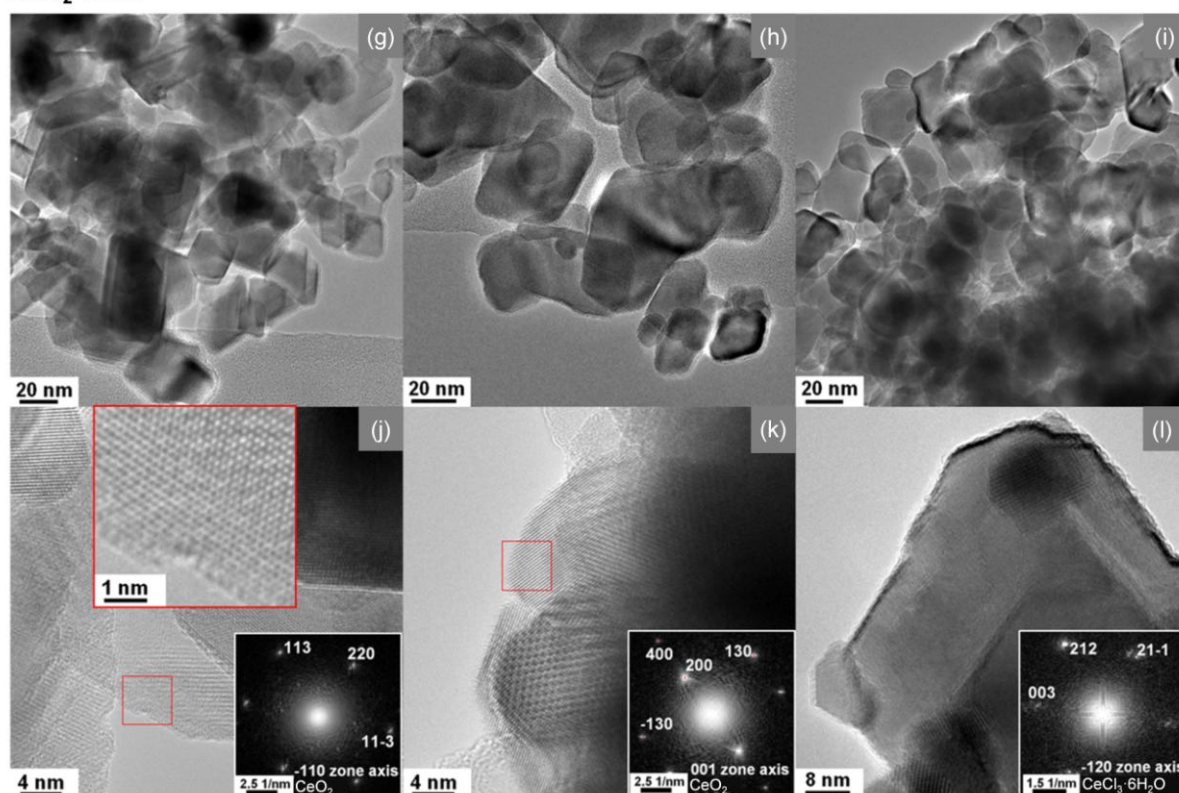


**Fig. 5.** TEM of (a) CeO<sub>2</sub>-773-F, (b) CeO<sub>2</sub>-773-2, (c) CeO<sub>2</sub>-773-0, and HRTEM of (d) CeO<sub>2</sub>-773-2, revealing the surface of the CeO<sub>2</sub> particles. (e) A CeO<sub>2</sub>-773-0 particle (surface termination in the inset) and (f) a CeO<sub>2</sub>-773-0 particle showing an amorphous layer of CeCl<sub>3</sub>·6H<sub>2</sub>O on the surface. TEM of (g) CeO<sub>2</sub>-1173-F, (h) CeO<sub>2</sub>-1173-2, and (i) CeO<sub>2</sub>-1173-0. Detailed imaging of (j) CeO<sub>2</sub>-1173-2, showing CeO<sub>2</sub> particles with clean surface (inset) and of (k,l) CeO<sub>2</sub>-1173-0, exhibiting both the (k) CeO<sub>2</sub> and (l) CeCl<sub>3</sub>·6H<sub>2</sub>O phases.



higher temperature, an effect that apparently occurred for the CeO<sub>2</sub>-773-F sample only after exposure to Deacon conditions. The only assigned phase in CeO<sub>2</sub>-1173-2 was CeO<sub>2</sub> (Fig. 5j). In CeO<sub>2</sub>-1173-0 both CeO<sub>2</sub> (Fig. 5k) and CeCl<sub>3</sub>·6H<sub>2</sub>O (Fig. 5l) were present. SAED analyses showed that CeO<sub>2</sub> is the dominant structure in the CeO<sub>2</sub>-1173-0 sample with a minor CeCl<sub>3</sub>·6H<sub>2</sub>O contribution. This result also agrees with X-ray diffraction (Fig. 4).

### 3.2.3. X-ray photoelectron spectroscopy

X-ray photoelectron spectroscopy was applied to selected catalysts to assess the degree of surface chlorination. Table 3 compiles the experimentally determined Cl/Ce ratios. In general, CeO<sub>2</sub>-773-F was more prone to chlorination than CeO<sub>2</sub>-1173-F. Moreover, exposure to HCl gave rise to a more extended chlorination than the exposure to HCl+O<sub>2</sub>. Both findings are in line with XRD analyses. To translate the Cl/Ce stoichiometry numbers that assume homogeneous distribution of Cl in the information depth into the number of near-surface layers containing Cl various models were applied (see details in the ESI). Thus, a more realistic layered structure was constructed (Cl occupation preference from top to down) giving rise to the same signal ratio as determined by XPS. As Table 3 indicates, Cl occupies approximately 1-1.5 layers in the samples used under Deacon conditions and 2.5 to 6 layers after HCl conditioning. Nevertheless, one should remember that after exposure to the mixture, the samples were quenched in N<sub>2</sub>, thus it is reasonable to assume that the Cl atoms adsorbed on external Ce atoms could desorb and hence are not counted in XPS. This assumption is in line with DFT simulations (Section 3.4.3). Based on the XPS data, it can be concluded that during the Deacon reaction, Cl atoms can occupy surface sites as well as lattice oxygen vacancies. This is in contrast to the RuO<sub>2</sub> case, where chlorination was confined to the surface layer [9,10,51]. Since XRD after HCl treatment detected traces of CeCl<sub>3</sub>·6H<sub>2</sub>O, the higher Cl uptake in the near-surface region for CeO<sub>2</sub>-1173-0 and CeO<sub>2</sub>-773-0 can be explained by the presence of the chloride phase. The Ce 3*d* difference spectrum (Fig. S10 in the ESI) between 773-0 and 773-F confirms the presence of CeCl<sub>3</sub>·6H<sub>2</sub>O. The calculation, indicating 8% of chloride phase (corresponding to an increase of Cl/Ce by ca. 0.24), is in relative good agreement with the observed increase in Cl/Ce by 0.36, and the difference might be due to additional sub-surface Cl occupation. In addition, Fig. S10 in the ESI suggests that calcination at 773 K is not sufficient to produce fully oxidized cerium (CeO<sub>2</sub>), an extra 10% of Ce<sup>3+</sup> state being estimated after this milder calcination.

**Table 3.** Quantification by different models of the surface Cl uptake from XPS measurements

Catalyst	Cl/Ce stoichiometry <sup>a</sup>	Number of layers occupied by Cl		
		Model 1	Model 2	Model 3
		IMFP <sup>b</sup>	EAL <sup>c</sup>	EAL, 75% Cl <sup>d</sup>
CeO <sub>2</sub> -773-F	-	-	-	-
CeO <sub>2</sub> -773-2	0.19	1.5	1.2	1.6
CeO <sub>2</sub> -773-0	0.55	5.7	4.6	6.1
CeO <sub>2</sub> -1173-F	-	-	-	-
CeO <sub>2</sub> -1173-2	0.14	1.0	0.8	1.1
CeO <sub>2</sub> -1373-0	0.29	2.4	1.9	2.6

<sup>a</sup> Based on homogeneous distribution of elements.

<sup>b</sup> Inelastic mean free path (by TPP-2M [50]); 22 Å.

<sup>c</sup> Effective attenuation length, 0.8×IMFP was used.

<sup>d</sup> Additionally to the EAL model, 75% Cl occupation of possible sites was considered, in line with the DFT calculations.

### 3.3. In situ Fourier transform infrared spectroscopy

In situ FTIR experiments were carried out to study the chlorination mechanism indirectly, that is, following the evolution of the OH stretching bands upon introducing a diluted Deacon feed. A detailed description of different configurations of H<sub>2</sub>O-related species adsorbed on CeO<sub>2</sub>(111) and the corresponding vibrational frequencies are presented in the ESI (Table S1). The CeO<sub>2</sub>-773-F sample was activated by heating in O<sub>2</sub>/N<sub>2</sub> up to 653 K, and holding at this temperature till no spectral changes were observed. The spectrum at the end of this stage (Fig. 6, dark blue) shows two main bands at 3713 and 3632 cm<sup>-1</sup>, which are respectively assigned to mono-coordinated (OH-I) and bridging (OH-IIB) hydroxyls [52-54]. Another absorption band at 3684 cm<sup>-1</sup>, due to water, as well as a band at 3660 cm<sup>-1</sup>, attributed to a different bridging hydroxyl species (OH-IIA), vanished during the activation process. The existence of two types of bridged hydroxyl groups was first reported by Badri et al. [52], who assigned the red-shifted band to bridged hydroxyl groups next to oxygen vacancies created by water elimination. According to our DFT calculations on CeO<sub>2</sub>(111), the mono-coordinate OH band should appear at 3729 cm<sup>-1</sup>, but threefold coordinated OH with surface O being part of the lattice can also give rise to bands in the range of 3750-3732 cm<sup>-1</sup>. Note that the calculation tends to overestimate the stretching frequency by 15-30 cm<sup>-1</sup>, when benchmarked with the same approaches for gas-phase water molecules. Additionally, OH-II species seem to be unstable on the (111) and (100) facets. On the other hand, bands related to water with a neighboring hydroxyl group are expected to fall around 3682-3646 cm<sup>-1</sup>; thus they may give rise to the low-frequency absorption.

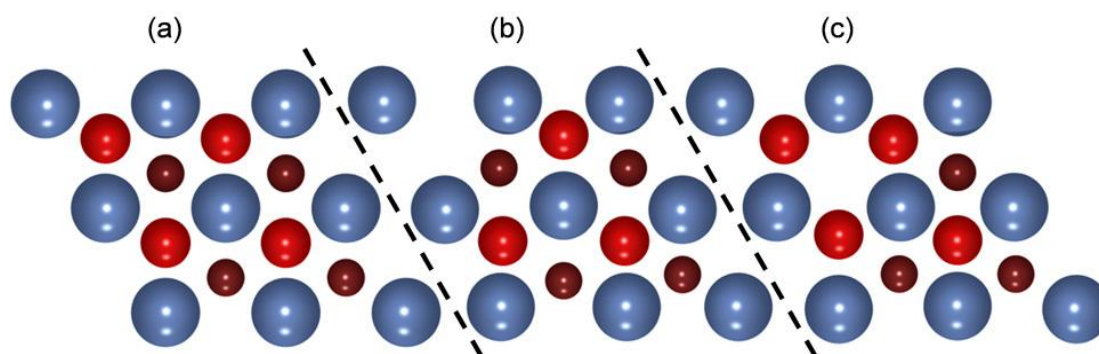


**Fig. 7.** Structural model of a  $p(2\times 2)$  supercell of  $\text{CeO}_2(111)$ : (a) regular surface, (b) surface vacancy, and (c) sub-surface vacancy. Ce atoms are depicted in blue, surface O atoms in red, and sub-surface O atoms in scarlet and small balls.

Two shoulders at  $3732\text{ cm}^{-1}$  and  $3702\text{ cm}^{-1}$  are visible on both sides of the high-frequency OH band. Upon introducing HCl in the  $\text{O}_2/\text{N}_2$  feed, these shoulders became more resolved. According to Table S1, they can be attributed to threefold coordinated hydroxyl groups, as well as to mono-coordinated OH groups with different neighboring species coexisting on the surface. During HCl oxidation, significant changes were observed in the spectra, as the intensity of the peak at  $3632\text{ cm}^{-1}$  decreased gradually till it was completely depleted at later stages (Fig. 6, light-blue till red). According to the bands assignment in the OH stretching region suggested by our DFT-calculated vibrational frequencies, this would indicate that the initial  $\text{H}_2\text{O}$ -OH pairs progressively disappeared, likely due to the partial occupation of the vacancies by Cl. OH-Cl pairs showed OH vibration at  $3739\text{ cm}^{-1}$ , just in the middle of the OH band of threefold and adsorbed OH. In parallel, the baseline in the whole spectral region first increased (light blue/brown/green), then declined to reach the level shown by the red spectrum. This modulation of the baseline reflects the rapid evolution, desorption, and stabilization of the hydrogen-bonded water structure as HCl dissociatively adsorbs on the ceria surface. The broad signal at  $3575\text{ cm}^{-1}$  (red spectrum), developed when the hydrogen-bonded water structure reached low enough concentration, can be assigned to isolated adsorbed water species produced during the reaction (in line with the theoretical value at  $3591\text{ cm}^{-1}$ ), since it diminished after stopping the HCl flow (black line). To visualize the changes occurring in the high-frequency OH band, the "HCl off" curve was subtracted from all other spectra. This illustration suggests that the changes in this band were not due to band shift, but rather related to the gradual disappearance of one OH species at  $3717\text{ cm}^{-1}$  in parallel with the depletion of the band at  $3632\text{ cm}^{-1}$ . This experiment suggests that surface chlorination occurs *via* dissociative HCl adsorption (baseline modulation) and consumption of OH groups, and thus through the displacement of surface oxygen species of different coordination by Cl.

### 3.4. Molecular modeling

#### 3.4.1. Vacancy formation, diffusion, and healing

The surface energy to cleave the (111) plane of  $\text{CeO}_2(111)$  is  $0.013\text{ eV \AA}^{-2}$ . The inward relaxation of the external atoms is  $0.090$  and  $0.097\text{ \AA}$  for Ce and O atoms, respectively. The material is known to be easily reducible and, thus, can accommodate oxygen vacancies [55]. The formation of surface vacancies, thereafter denoted as  $\square$ , in  $0.25\text{ ML}$  (monolayers) in the  $p(2\times 2)$  cell is endothermic by  $3.25\text{ eV}$ . This is a very small value when compared to ionic materials [56] or to other reducible oxides like  $\text{SrTiO}_3$  [57]. The electronic structure of the surface vacancy corresponds to an anti-ferromagnetic solution, where the two electrons left end up in the next and next nearest surface Ce atoms, as described by Ganduglia-Pirovano et al. [43]. The electronic structure, electron localization, and formation energy are in good agreement with previous calculations with both PBE+U and HSE06 functionals [43]. The latter is supposed to be more accurate for strongly localized *f*-electrons. However, the energy difference with other configurations is rather small and dynamic re-ordering of the electronic structure through polaronic effects is likely to occur [58,59].

Oxygen vacancies can be present in near-surface layers (Fig. 7c). Indeed, the formation energy for sub-surface defects turns out to be lower than for surface defects,  $2.93\text{ eV}$ , in agreement with previous theoretical estimates [43]. The energy requirement for surface to sub-surface vacancy diffusion is small,  $0.30\text{ eV}$ , in line with reported values for bulk diffusion,  $0.50\text{ eV}$  [60]. Vacancy agglomeration has also been evidenced by scanning tunneling microscopy (STM) investigations [28]. From our calculations on a  $p(4\times 2)$  supercell, surface vacancy agglomeration at a constant concentration of  $0.25\text{ ML}$  is weakly exothermic, by  $0.13\text{ eV}$ , in agreement with STM images.

As for the surface re-oxidation, oxygen adsorption does not take place on a non-defective  $\text{CeO}_2(111)$  surface, but occurs on surface oxygen vacancies,  $\square$ , leading to a

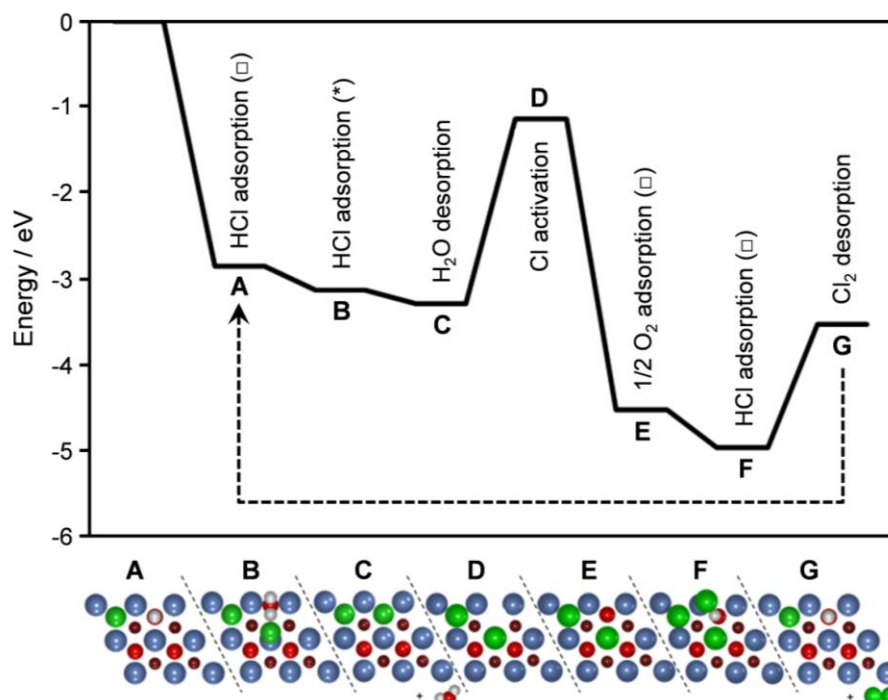


**Fig. 8.** Reaction energy profile for the Deacon process on CeO<sub>2</sub>(111). The initial state in the profile is CeO<sub>2</sub>(111) with a surface oxygen vacancy. The color codes in the bottom panels are as described in the caption of Figure 7.

superoxo-like species, in which one of the two O atoms fills the hole, and the O-O distance is 1.453 Å. Dissociation of this bond heals the defect and leaves a surface O atom, but it is uphill by 1.80 eV. Nevertheless, the dynamics of oxygen vacancies in oxides can be enhanced by the presence of gas-phase O<sub>2</sub> [61]. Aggregation of oxygen defects at the surface or near-surface is energetically favored. Indeed, surface vacancy diffusion takes place by penetration to the sub-surface layer and ejection towards the surface in neighboring lattice position. The first step is exothermic by 0.72 eV with a barrier of 0.24 eV, while the second is mildly endothermic (0.59 eV) with a barrier of 0.64 eV. Once the defect dimer is present on the surface, gas-phase oxygen molecules can interact healing both vacancies and liberating about 6 eV.

### 3.4.2. Chlorination

In order to assess the stability of CeO<sub>2</sub>(111), we have employed first-principles thermodynamics [62] to consider the effect of partial oxygen and chlorine pressures on the state of the surface. The stability problem is considerable and was simplified by exclusively considering a reactant (O<sub>2</sub>) and a product (Cl<sub>2</sub>), for which no crossing between the associated chemical potentials appears in the equations. The excess surface energy can be calculated from Eq. (3):

$$\Delta G_X \approx E_X - E_{\text{CeO}_2} + N_{\text{O}_2}/2 \mu_{\text{O}_2} - N_{\text{Cl}_2}/2 \mu_{\text{Cl}_2} \quad (3)$$

where  $\Delta G_X$  is the Gibbs energy associated with the configuration X with respect to the energy of regularly terminated CeO<sub>2</sub>,  $E_{\text{CeO}_2}$ ,  $N_{\text{O}_2}$  and  $N_{\text{Cl}_2}$  are the number of oxygen and chlorine molecules, and  $\mu$  is the corresponding gas-phase chemical potential. The ability of HCl to form chlorides is somehow higher than that of Cl<sub>2</sub>, but the present model serves as a guide to evaluate the degree of chlorination of the material. The Gibbs potentials of solids including 40 different X configurations,  $E_X$ , and of the regular surface,  $E_{\text{CeO}_2}$ , were taken from DFT calculations and the chemical potentials of Cl<sub>2</sub> and O<sub>2</sub> were calculated through statistical thermodynamics [63]. Fig. S11 in the ESI shows that, at extremely low oxygen and chlorine chemical potentials, the surface is regularly terminated. When increasing the Cl<sub>2</sub> pressure, partial chlorination can take place by substitution of an oxygen atom from the surface (Fig. S11 in the ESI, green configuration). At relatively low oxygen pressures (for  $\log(p_{\text{O}_2})$  and  $\log(p_{\text{Cl}_2})$  in the range -1-2), the clean surface, mono-substituted Cl, and multiple substituted Cl structures lie very close in energy and are likely present in the catalyst surface. If the chlorine pressure is much higher ( $\log(p_{\text{Cl}_2}) = 0$ ), lattices with Cl in oxygen positions become more stable. The maximum oxygen substitution achievable in this way corresponds to 50% of the surface oxygen atoms. If the oxygen pressure is raised up to the 0.1 bar regime, as in our catalytic tests, then the most likely configuration corresponds to the clean surface. Finally, the thermodynamic penalty to introduce a

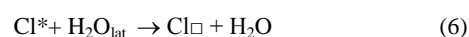
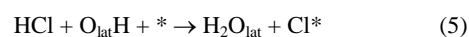
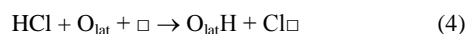
Cl atom occupying a vacancy site (Cl $\square$ ) to inner layers is about 3 eV. Accordingly, it is implied that Cl preferentially stays in the near-surface region, and that high HCl or Cl<sub>2</sub> pressures might account for lattice disruption and formation of CeCl<sub>3</sub>-related phases (Section 3.2), as Cl cannot be accommodated in the bulk of CeO<sub>2</sub>.

### 3.4.3. Reaction mechanism

The reaction profile of the HCl oxidation on CeO<sub>2</sub> is presented in Fig. 8. The main elementary steps derived for the Deacon process comprise: (i) hydrogen abstraction from HCl by basic surface O atoms, to form hydroxyl groups and leave chlorine atoms on the surface, (ii) reaction of the hydroxyl groups with new incoming HCl molecules and/or hydroxyl group recombination on the surface to form water, (iii) water removal, (iv) re-oxidation, and (v) recombination of chlorine atoms.

The Deacon reaction starts by the adsorption of HCl near the basic centers on the surface (lattice oxygen atoms, O<sub>lat</sub>). The reaction is energetically favored provided that a surface vacancy exists, where the Cl atom can be accommodated (Fig. 8, step A). In this process, HCl adsorption is exothermic by 2.84 eV and leads to a surface O<sub>lat</sub>H group and a Cl atom at the surface vacancy. Care should be taken as both O<sub>lat</sub> and adsorbed O atoms can give rise to the OH-I and OH-II vibrational bands described in Section 3.3. At the transition state, the H-Cl and O<sub>lat</sub>-H distances are 3.590 and 2.121 Å, respectively. A second HCl molecule can adsorb, forming a water molecule and leaving a Cl atom on top of a Ce atom on the surface, Cl\* (Fig. 8, step B). This second process is also exothermic, but only by 0.29 eV. The external Cl\* atom can push the already formed water molecule H<sub>2</sub>O<sub>lat</sub> out of the lattice and fill the nascent vacancy, thus becoming Cl $\square$ . This process is almost thermo-neutral (Fig. 8, step C). Then, one of the oxygen atoms from the sub-surface layer can diffuse towards the surface, pushing a Cl $\square$  atom towards the outer surface, i.e. converting Cl $\square$  in Cl\* (Fig. 8, step D). The energy required for this elementary step is 2.15 eV and forms an oxygen vacancy at a subsurface position,  $\square_{ss}$ . Re-oxidation can take place by the complex diffusion-reaction mechanism described in Section 3.4.1 to release nearly 3.4 eV (Fig. 8, step E). Still, HCl can adsorb on this surface releasing 0.42 eV to form a O<sub>lat</sub>H and a Cl\* (Fig. 8, step F). Three chlorine atoms are then adsorbed on the surface, one Cl\* and two Cl $\square$ , respectively. Cl<sub>2</sub> evolution towards the gas-phase takes place from this structure; the energy required is 1.42 eV (Fig. 8, step G). As it can be noticed in Fig. 8, states A and G correspond to the active states of the catalyst. Therefore, the catalytic cycle runs between steps A and G.

The list of elementary steps in the mechanism can be summarized by the following reactions:



It is important to notice that, although the reaction scheme on CeO<sub>2</sub> resembles that of RuO<sub>2</sub>, some important differences are found. First, the reaction on RuO<sub>2</sub> occurs at almost full coverage of the under-coordinated Ru<sub>cus</sub> positions, as nearly all available sites are occupied by Cl [9]. For CeO<sub>2</sub>, under-coordinated cerium atoms only exist when oxygen vacancies are present in the surface or near-surface regions. These are the only active sites for the reaction, in agreement with the linearity found between activity and OSC (Fig. 1b). As a consequence, the reaction profile for CeO<sub>2</sub> is much more abrupt (involves higher energy requirements) than that of RuO<sub>2</sub>. This correlates with the higher temperatures needed to run the Deacon reaction on CeO<sub>2</sub> (vide supra). The most energy-demanding step of HCl oxidation on RuO<sub>2</sub> is related to the formation and evolution of Cl<sub>2</sub>. Due to the high energy required for Cl<sub>2</sub> elimination on RuO<sub>2</sub>, Cl self-poisoning is observed and, thus, re-oxidation turns out to be the major obstacle (rate-determining step) for the whole reaction at relevant conditions, as shown by the positive dependence of the activity on the partial pressure of O<sub>2</sub> [51]. For CeO<sub>2</sub>, the activation of Cl atoms from lattice vacancies to surface positions is the most energy-demanding step.

The similar activity enhancement observed at higher partial O<sub>2</sub> pressures (Fig. 2) can be rationalized on the basis of the chlorine and oxygen competition for the same active sites, which tightly couples chlorine elimination to oxygen re-adsorption. When Cl atoms occupy most of the active positions, very few active sites exist for re-oxidation, thus producing less Cl<sub>2</sub>. In extreme cases, this leads to catalyst deactivation.

Regarding the stability against the harsh reaction conditions employed, while the experimental data indicate that RuO<sub>2</sub> and CeO<sub>2</sub> are quite similar, the DFT analysis points out some differences. The RuO<sub>2</sub> surface is known to be partially chlorinated, but this chlorination is confined to the under-coordinated O and Ru positions at the external surface. Comparing surface Cl contents, the situation is such that the amount of Cl on the surface of RuO<sub>2</sub> is very large, as the under-coordinated positions in the lattice are very prone to adsorb reactants (Cl in particular). This effect is less evident on CeO<sub>2</sub>, given the relative inertness of Ce atoms on the surface. Indeed, most of the Cl is sitting at oxygen vacancies on the surface and not directly on top of the active Ce sites. In addition, the penetration of Cl atoms to deeper layers is hindered in both RuO<sub>2</sub> and CeO<sub>2</sub> systems by more than 2 eV. This energy is somewhat larger

**Table 4.** Energy ( $\Delta E$ ) in eV and Gibbs free energy ( $\Delta G^0$ ) in kJ mol<sup>-1</sup> M (M = Ce, Ru) atom for the complete chlorination of CeO<sub>2</sub> and RuO<sub>2</sub> by Cl<sub>2</sub> or HCl.<sup>a</sup>

Chlorination equation	$\Delta E$	$\Delta G^0$	
		573 K	703 K
CeO <sub>2</sub> + 3/2Cl <sub>2</sub> → CeCl <sub>3</sub> + O <sub>2</sub>	15.82	92.95	112.18
CeO <sub>2</sub> + 4HCl → CeCl <sub>3</sub> + 2H <sub>2</sub> O + 1/2Cl <sub>2</sub>	-115.99	60.61	97.95
RuO <sub>2</sub> + 3/2Cl <sub>2</sub> → RuCl <sub>3</sub> + O <sub>2</sub>	101.86	178.98	198.22
RuO <sub>2</sub> + 4HCl → RuCl <sub>3</sub> + 2H <sub>2</sub> O + 1/2Cl <sub>2</sub>	-29.95	146.65	183.98

<sup>a</sup> Calculated using the PBE (RuO<sub>2</sub>) and PBE+U (CeO<sub>2</sub>) functionals

for CeO<sub>2</sub> (3 eV). Nevertheless, owing to vacancy diffusion, and thus oxygen supply to the surface, ceria will be more prone to sub-surface and bulk chlorination in pure HCl or sub-stoichiometric Deacon feeds. In line with this, we have compared the energy required for the bulk chlorination and lattice disruption in both Ru and Ce cases, see Table 4. The energy requirement for the chlorination of CeO<sub>2</sub> is smaller than the corresponding value for RuO<sub>2</sub>, in agreement with the greater chlorination detected in the CeO<sub>2</sub> experiments in HCl-rich feeds.

## 4. Conclusions

In this study we present a fundamental understanding of HCl oxidation on bulk CeO<sub>2</sub> combining catalyst testing, steady-state kinetics, characterization, and DFT simulations. CeO<sub>2</sub> is proven remarkably active and stable, constituting a promising alternative to highly expensive RuO<sub>2</sub>-

based catalysts for industrial chlorine recycling. The activity is related to the presence of oxygen vacancies in the material. The stability arises from the remarkable resistance of cerium oxide against chlorination. Limited bulk chlorination, that is detection of CeCl<sub>3</sub> by X-ray diffraction, takes place under HCl-rich conditions (O<sub>2</sub>/HCl ≤ 0.25). The bulk chloride phase rapid and completely disappears when the catalyst is exposed to O<sub>2</sub>-rich conditions. Under O<sub>2</sub>/HCl ≥ 0.75, only the outermost surface layers of CeO<sub>2</sub> contain chlorine. Density functional theory simulations reveal that Cl activation from vacancy positions to surface Ce atoms is the most energy-demanding step, although chlorine-oxygen competition for the available active sites may render re-oxidation as the rate-determining step. Current studies focus on developing a proper strategy to support the active phase on a suitable carrier preserving the remarkable stability of bulk CeO<sub>2</sub>.

## Acknowledgements

We thank Bayer MaterialScience for permission to publish these results.

**Electronic Supplementary Information (ESI):** Experimental details of the applied characterization techniques, additional results from characterization, catalytic testing, and DFT simulations. The above material is available at <http://www.sciencedirect.com>.

## References

- [1] J. Pérez-Ramírez, C. Mondelli, T. Schmidt, O.F.-K. Schlüter, A. Wolf, L. Mleczko, T. Dreier, Energy Environ. Sci. (2011) DOI:10.1039/C1EE02190G.
- [2] K. Seki, Catal. Surv. Asia 14 (2010) 168.
- [3] H. Deacon, U.S. Patent 85,370, 1868, assigned to Gaskell, Deacon and Co.
- [4] A.J. Johnson, A.J. Cherniavsky, U.S. Patent 2,542,961, 1951, assigned to Shell Development Company.
- [5] T. Kiyoura, N. Fujimoto, M. Ajioka, T. Suzuki, Y. Kogure, K. Kanaya, T. Nagayama, EP184413-A, 1984, assigned to Mitsui Chemicals.
- [6] T. Hibi, H. Nishida, H. Abekawa, U.S. Patent 5,871,707, 1999, assigned to Sumitomo Chemical Company.
- [7] C. Mondelli, A.P. Amrute, F. Krumeich, T. Schmidt, J. Pérez-Ramírez, ChemCatChem 3 (2011) 657.
- [8] A. Wolf, L. Mleczko, O.F. Schlüter, S. Schubert, EP2026905, 2006, assigned to Bayer Material Science.
- [9] M.A.G Hevia, A.P. Amrute, T. Schmidt, J. Pérez-Ramírez, J. Catal. 276 (2010) 141.
- [10] D. Crihan, M. Knapp, S. Zweidinger, E. Lundgren, C.J. Weststrate, J.N. Andersen, A.P. Seitsonen, H. Over, Angew. Chem. Int. Ed. 47 (2008) 2131.
- [11] J.P. Hofmann, S. Zweidinger, A.P. Seitsonen, A. Farkas, M. Knapp, O. Balmes, E. Lundgren, J.N. Andersen, H. Over, Phys. Chem. Chem. Phys. 12 (2010) 15358.
- [12] Retrieved from <http://www.platinum.matthey.com/pgm-prices>.
- [13] C. Mondelli, A.P. Amrute, T. Schmidt, J. Pérez-Ramírez, Chem. Commun. (2011) 7173.
- [14] R.W.G. Wyckoff, Crystal Structures, Interscience, New York, 1965.
- [15] R.J. Gorte, AIChE J. 56 (2010) 1126.
- [16] Q. Fu, H. Saltsburg, M. Flytzani-Stephanopoulos, Science 301 (2003) 935.
- [17] A. Primo, T. Marino, A. Corma, R. Molinari, H. Garcia, J. Am. Chem. Soc. 133 (2011) 6930.
- [18] Y.S. Chaudhary, S. Panigrahi, S. Nayak, B. Sarpati, S. Bhattacharjee, N. Kulkarni, J. Mater. Chem. 20 (2010) 2381.
- [19] M. Mogensen, N.M. Sammes, G.A. Tompsett, Solid State Ionics 129 (2000) 63.
- [20] B. Zhu, M.D. Mat, Int. J. Electrochem. Sci. 1 (2006) 383.
- [21] F. Zhou, X. Zhao, H. Xu, C. Yuan, J. Phys. Chem. C 111 (2007) 1651.



- [22] A. Trovarelli, Catal. Rev. -Sci. Eng. 38 (1996) 439.
- [23] A. Gómez-Cortés, Y. Márquez, J. Arenas-Alatorre, G. Díaz, Catal. Today 133-135 (2008) 743.
- [24] A. Martínez-Arias, A.B. Hungria, G. Munuera, D. Gamarra, Appl. Catal., B 65 (2006) 207.
- [25] W. Shin, C. Jung, J. Han, S. Nam, T. Lim, S Hong, H. Lee, J. Ind. Eng. Chem. 10 (2004) 302.
- [26] T.X.T. Sayle, S.C. Parker, C.R.A. Catlow, Surf. Sci. 316 (1994) 329.
- [27] H.C. Yao, Y.F.Y. Yao, J. Catal. 86 (1984) 254.
- [28] F. Esch, S. Fabris, L. Zhou, T. Montini, C. Africh, P. Fornasiero, G. Comelli, R. Rosei, Science 309 (2005) 752.
- [29] N. Laosiripojana, W. Sutthisripok, P. Kim-Lohsoontorn, S. Assabumrungrat, Int. J. Hydrogen Energy 35 (2010) 6747.
- [30] R. Di Monte, J. Kašpar, Top. Catal. 28 (2004) 47.
- [31] A. Hagemeyer, P. Trübenbach, C.W. Rieker, M. Wunsch, O. Watzemberger, EP patent 0761594-A1, 1997.
- [32] A. Wolf, L. Mleczko, O.F. Schlüter, S. Schubert, WO2010133313-A1, 2010.
- [33] G. Lee, S.W. Lee, I. Sohn, Y.C. Kwon, J. Song, C.-S. Son, WO2009035234-A2, 2009.
- [34] G. Dutta, U.V. Waghmare, T. Baidya, M.S. Hegde, K.R. Priolkar, P.R. Sarode, Chem. Mater. 18 (2006) 3249.
- [35] G.R. Rao, B.G. Mishra, Bull. Catal. Soc. India 2 (2003) 122.
- [36] H.A. Al-Madfaa, M.M. Khader, Mater. Chem. Phys. 86 (2004) 180.
- [37] B.M. Reddy, P. Bharali, P. Saikia, J. Phys. Chem. C 112 (2008) 11729.
- [38] F. Deganello, A. Martorana, J. Solid State Chem. 163 (2002) 527.
- [39] A.P. Amrute, C. Mondelli, M.A.G. Hevia, J. Pérez-Ramírez, J. Phys. Chem. C 115 (2011) 1056.
- [40] G. Kresse, J. Hafner, Phys. Rev. B 47 (1993) 558.
- [41] J.-P. Perdew, K. Burke, M. Ernzerhof, Phys. Rev. Lett. 77 (1996) 3865.
- [42] M. Cococcioni, S. Gironcoli, Phys. Rev. B. 71 (2005) 035105 and references therein.
- [43] M.V. Ganduglia-Pirovano, J.L.F. Da Silva, J. Sauer, Phys. Rev. Lett. 102 (2009) 026101 and references therein.
- [44] P.E. Blöchl, Phys. Rev. B 50 (1994) 17953.
- [45] H.J. Monkhorst, J.D. Pack, Phys. Rev. B 13 (1976) 5188.
- [46] G. Henkelman, B.P. Uberuaga, H. Jonsson, J. Chem. Phys. 113 (2000) 9901.
- [47] D. Terribile, A. Trovarelli, C. de Leitenburg, G. Dolcetti, J. Llorca, Chem. Mater. 9 (1997) 2676.
- [48] M.W.M. Hisham, S.W. Benson, J. Phys. Chem. 99 (1995) 6194.
- [49] A.P. Amrute, C. Mondelli, M.A.G. Hevia, J. Pérez-Ramírez, ACS Catal. 1 (2011) 583.
- [50] S. Tanuma, C.J. Powell, D.R. Penn, Surf. Interface Anal. 21 (1994) 165.
- [51] D. Teschner, R. Farra, L.-D. Yao, R. Schlogl, H. Soerijanto, R. Schomaecker, T. Schmidt, L. Szentmiklósi, A.P. Amrute, C. Mondelli, J. Pérez-Ramírez, G. Novell-Leruth, N. Lopez, J. Catal. (2011), DOI:10.1016/j.jcat.2011.09.039.
- [52] A. Badri, C. Binet, J. Lavalley, Faraday Trans. 92 (1996) 4669.
- [53] A. Laachir, V. Perrichon, A. Badri, J. Lamotte, E. Catherine, J.C. Lavalley, J. El Fallah, L. Hilaire, F. Le Normand, E.E. Quéméré, G.N. Sauvion, O. Touret, Faraday Trans. 87 (1991) 1601.
- [54] C. Binet, M. Daturi, J. Lavalley, Catal. Today 50 (1999) 207.
- [55] T.B. Lindemer, J. Brynstad, J. Am. Ceram. Soc. 69 (1986) 867.
- [56] J. Carrasco, N. Lopez, F. Illas, Phys. Rev. Lett. 93 (2004) 225502.
- [57] J. Carrasco, F. Illas, N. Lopez, E.A. Kotomin, Y.F. Zhukovskii, R.A. Evarestov, Y.A. Mastrikov, S. Piskunov, J. Maier, Phys. Rev. B. 73 (2006) 064106.
- [58] P.M. Kowalski, M.F. Camellone, N.N. Nair, B. Meyer, D. Marx, Phys. Rev. Lett. 105 (2010) 146405.
- [59] S. Chretien, H. Metiu, J. Phys. Chem. C 115 (2011) 4696.
- [60] P.P. Dholabhai, J.B. Adams, P. Crozier, R. Sharma, J. Chem. Phys. 132 (2010) 094104.
- [61] N. Lopez, J.D. Prades, F. Hernandez-Ramirez, J.R. Morante, J. Pan, S. Mathur, Phys. Chem. Chem. Phys. 12 (2010) 2401.
- [62] X.G. Wang, A. Chaka, M. Scheffler, Phys. Rev. Lett. 84 (2000) 3650.
- [63] D.A. McQuarrie, J.D. Simon, Molecular Thermodynamics, University Science Books, Sausalito California, 1999.